6th International Meeting
on
Wind Turbine Noise
Glasgow 20-13 April 2015

Simulation of broadband Trailing-Edge Noise – Influence of Airfoil Shape and Flow Characteristics

Christof Rautmann - German Aerospace Center (DLR)
Lilienthalplatz 7, 38108 Braunschweig, Germany
christof.rautmann@dlr.de

Roland Ewert - German Aerospace Center (DLR)
Lilienthalplatz 7, 38108 Braunschweig, Germany
roland.ewert@dlr.de

Jürgen Dierke - German Aerospace Center (DLR)
Lilienthalplatz 7, 38108 Braunschweig, Germany
juergen.dierke@dlr.de

Summary

Broadband turbulent boundary layer trailing-edge noise (TBL-TEN) is the dominant noise source for new generation multi-Megawatt wind turbines operating in rated condition or below. The evaluation of the radiated noise in the rotor blade design process is quite challenging. Different prediction methods are known, ranging from fast and simple semi-empirical models to long-lasting and resource-intensive direct numerical simulations. This paper presents a fast and powerful noise simulation method for the broadband two-dimensional airfoil TEN issue. A combined approach is used, where a steady state computational fluid dynamics (CFD) simulation commits mean flow values to a subsequent computational aeroacoustic (CAA) simulation. The fluctuating turbulent noise sources are reconstructed from the RANS (Reynolds-averaged Navier-Stokes) turbulence statistics by a stochastic method. Compared to scale resolving simulations, this effectively reduces the effort on the flow simulation side. The result is a time and space resolved sound field around the 2D airfoil which can be used for various evaluations. As the validation of this method could be shown in former publications, the CFD/CAA approach is now used to predict the noise radiation of arbitrary airfoils. A systematic approach of airfoil shape variation is undertaken to identify the main noise drivers. A quite common wind turbine airfoil (DU-96-W-180) is chosen as baseline geometry, which is then modified in camber and thickness. The effects on aerodynamic and aeroacoustic performance are analyzed. Moreover the influence of forced laminar turbulent transition on the airfoils sound emission is investigated with the combined CFD/CAA method.

1 Introduction

As energy politics in Europe and around the world tend to shift progressively towards greener and renewable energy sources, increasing numbers of wind turbines become apparent in today's environment. At the end of 2013 a global total of 318 GW of wind capacity was installed, representing a cumulative annual growth rate of 12.5 % [1]. Especially in Europe (117 GW installed capacity, cumulative growth rate 10.0 % [2]) where the onshore sector (94 %) still represent the biggest share and the space for wind farms is limited, turbines are moving closer to inhabited areas. Together with growing rotor dimensions of new turbine generations not only aesthetic concerns arise, but also noise becomes an issue. This happens particularly in rural areas which used to be very quite. Consequently, noise regulations govern the noise emissions of turbines, distances to residents or timeframes of wind farm operations. So, from a wind farm operator point of view low noise turbines might be more profitable. It is therefore the task of a turbine manufacturer or designer to incorporate the acoustic design challenges into the development process. Hence, precise acoustic evaluation tools and methods are needed.
Beside mechanical noise in the turbines nacelle different flow-induced noise mechanisms can be distinguished for the rotor blades airfoils[3, 4], e.g. turbulent inflow noise, tip vortex formation noise, blunt trailing-edge vortex shedding noise, separation noise and turbulent boundary layer trailing-edge noise (TBL-TEN). Different studies on wind turbine noise[5] have shown that TBL-TEN is the dominant noise source for modern wind turbines. This finding is further underlined by tests with trailing-edge devices which showed good results in reducing TBL-TEN and thereby the overall levels [6, 7, 8]. As TBL-TEN scales with the fifth power of the relative flow velocity[9], the outer parts of the rotor with high relative velocities are most of interest. Aside from noise, aerodynamic design constraints need to be considered in this region, as most of the rotors torque is produced here. Therefore changes in airfoil geometry must be analyzed against the backdrop of aerodynamic as well as acoustic performance.
Depending on the complexity of the noise prediction problem, different prediction approaches are known (see Fig. 1). The simplest and fastest approach is to use a semi-empirical method (e.g. the method proposed by Brooks, Pope and Marcolini[3] - BPM method) to determine TBL-TEN based on boundary layer parameters and acoustic measurements from reference airfoils. As this technique is based on measurements from NACA airfoils, it is prone to inaccuracy when applied to arbitrary airfoils with a geometrical shape significantly different from a NACA0012. A considerable level of simplification is introduced into the prediction and does not allow taking into account the full geometrical and flow complexity that might be present.
In contrast to that, scale resolving simulations like Large Eddy Simulation (LES) approaches could provide a clearer insight into the turbulent flow problem that underlies the aeroacoustic sound generation process and as such yield the best level of physical modeling of the problem. For that purpose the Navier-Stokes equations are solved directly and only with the modest additional assumptions leading to a very high computational effort. Even on modern high-performance clusters computation times are out of reach for the simulation of complex flow problems for industrial application.
Stochastic approaches might bridge the gap between scale resolving methods and semi-empirical approaches. Herein a time-averaged solution of the RANS equations is used to prescribe the turbulent flow problem. Unsteady sound sources must be reconstructed from the turbulence statistics, which is in general incomplete as it lacks

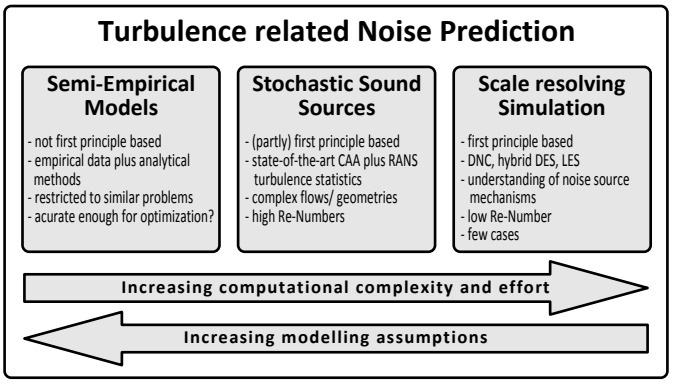

Figure 1: Turbulence related noise prediction methods.

some information about the turbulence, e.g. the complete length scale anisotropy tensor. Nevertheless, the RANS information might be sufficient for a proper prediction of aeroacoustic trends even for perhaps relatively subtle changes in the problem statement such as flow velocity, angle of attack (AoA), or geometrical changes. Stochastic approaches have the advantage of being computational more efficient than scale resolving simulation and as such allow to simulate full-scale high Reynolds number problems or a greater number of modifications in an aeroacoustic design process.
For the present paper, the combined CFD/CAA approach with stochastic source reconstruction is used to predict the trailing-edge noise from a DU-96-W-180 airfoil. A systematic geometry variation similar to the 4-digti-NACA airfoil-series variation of thickness and camber is used to study the effect of different geometries on the emitted noise spectrum from the airfoil. Together with the full range of CFD and CAA data a combined aerodynamic and aeroacoustic assessment for the different airfoils is made. In addition to the geometrical variations the influence of laminar-turbulent boundary layer transition is studied and its effect on noise is classified.
First, the numerical methods and theories are presented in Section 2. Setup and geometry for the different test cases are prescribed in Section 3 and the results are shown and discussed in Section 4.

2 Numerical Setup

2.1 Aeroacoustic Tool Chain

The broadband trailing-edge noise prediction is done in a first-principle based hybrid procedure comprising two basic steps (see Fig. 2). Step one is the simulation of the time-averaged turbulent flow field around the airfoil. Therefore a well established RANS CFD simulation is conducted. In a rotor blade design process this simulation might already exist due to preliminary aerodynamic investigations. So, a dual use of the data is possible, if the turbulent boundary layer is correctly resolved. Step two is the computational aeroacoustic simulation for the flow problem, where linear perturbation equations are solved, which yields the time and space resolved sound pressure field around the airfoil. The steady RANS simulation from step one thereby provides the mean-flow field over which the aeroacoustic simulation is conducted. In an intermediate step the unsteady turbulent vortex sound sources are reconstructed from the time-averaged

RANS turbulence statistics by a stochastic reconstruction procedure called Fast Random Particle Mesh Method (FRPM)[10, 11].

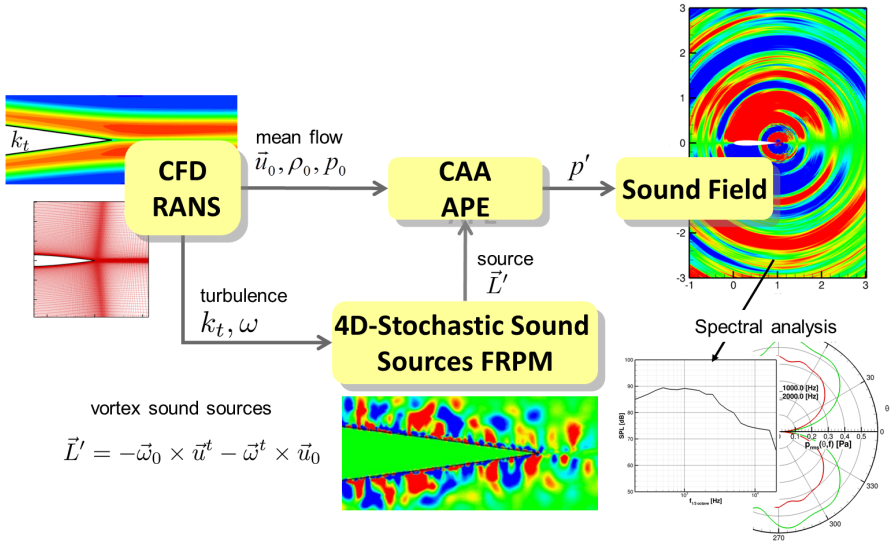

Figure 2: Schematic of CAA prediction method of DLR based on a two-step hybrid method using a steady RANS CFD step, followed by a CAA step solving Acoustic Perturbation Equations (APE); the generation of fluctuating turbulent sound sources is realized with the 4-D FRPM synthetic turbulence method.

In the present study multiple geometries and flow parameters will be analyzed. It is therefore essential to automize most of the steps in the aeroacoustic tool chain. Starting from the X and Y coordinates of the airfoil under investigation meshes for the CFD simulation automatically created. Moreover the simulation is started by a script and after a successful run necessary data for the follow-on CAA steps is post-processed and interpolated onto the CAA mesh. The CAA mesh itself is also generated automatically using the same airfoil geometry as for the CFD mesh. Through the excessive use of scripts and replay files most of the manual work in the aerodynamic and acoustic evaluation could be saved. Nevertheless physical plausibility and result quality where regularly checked to ensure high quality final results. The number of simulated designs could be increased with the time savings gained by the automation procedure. Further details of the particular steps are provided in the following subsections.

2.2 CFD

As detailed flow information are needed for the subsequent CAA and FRPM steps a 2D CFD simulation for each airfoil geometry and flow setting is conducted. The flow vector information ($\boldsymbol{u}$) as well as pressure (p) and density (ρ) distributions around the airfoil are needed to build the underlying mean-flow field for the CAA simulation over which the sound waves emerging from the trailing-edge are propagated. Turbulence statistics from the used two equation k-ω model are needed for the turbulence reconstruction step in FRPM (see Sec. 2.4). The simulations were carried out using the unstructured DLR in-house CFD solver TAU[12, 13]. Note, that each other CFD solver (commercial or open-source) might also be suitable for the simulations as far as the prescribed flow values and turbulence statistics can be calculated.

For each airfoil a two-dimensional computational domain is generated using the commercial grid generator ICEM CFD. With the use of replay-scripts it was possible to automate all steps of the mesh creation. In this way a consistent meshing approach with almost unvarying quality could be granted for all geometries. The domains outer boundaries extend about 100 chord lengths around the airfoil to prevent unphysical interferences of the boundary conditions with the near airfoil flow. A hybrid grid is chosen, where the viscous sub-layer is resolved by a structured region and areas far away from the airfoil are resolved by a coarser quad-dominated unstructured grid. Throughout the airfoil surface 225 nodes are distributed along the upper and lower side respectively. The height of the first cell layer is determined so, that a dimensionless wall distance of $y^+ < 1$ is achieved. Hence, the boundary layer is directly resolved by the turbulence model and no wall-functions are required for near-wall modeling. The structured near-airfoil grid extends about 110 layers from the wall with an exponential growth factor of 1.1. Thus, a good resolution of the viscous sub-layer is realized and the numerical error is reduced. Moreover the near airfoil blocks are distributed such, that almost perpendicular cells are generated at the airfoil wall. Block corners are positioned with respect to the airfoil geometry by the replay script to account for changes of the geometry. The hybrid structured/unstructured meshing approach reduces cell density in less interesting areas away from the airfoil and cuts the total number of grid cells down to approximately 100k.
As an example the baseline DU-96-W-180 grid, normalized by the chord lengths l_c is shown in Fig. 3 (a). The structured region in the vicinity of the airfoil is shown in Fig. 3 (b) and the mesh resolution close to the wall can be seen in detail in (c). The same blocking strategy and meshing procedure was used for all airfoils in this study.

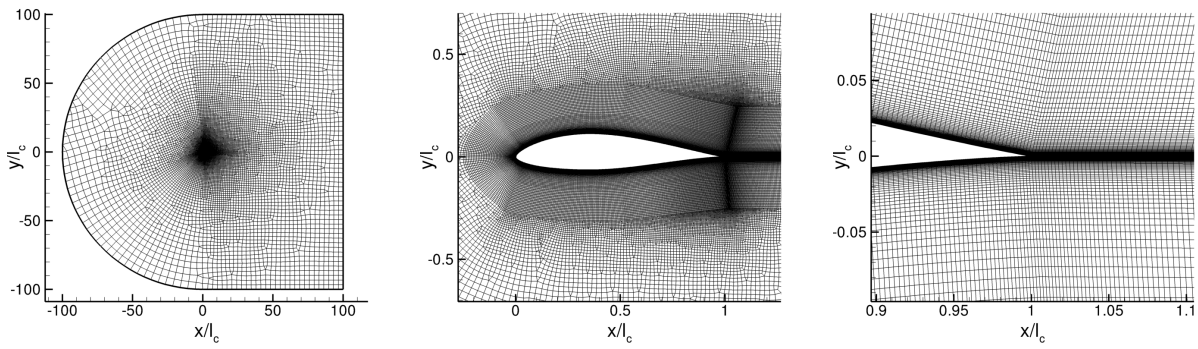

(a) (b) (c)

Figure 3: Baseline DU-96-W-180 airfoil with hybrid structured/unstructured CFD mesh around the airfoil; (a) domain overview; (b) structured near airfoil region; (c) cells in the vicinity of the trailing-edge.

The airfoils suction and pressure side are defined as viscous walls. For all calculations with fixed laminar-turbulent transition, the transition location is set to $x_{tr} = x/l_c = 0.12$ on the airfoils suction side and $x_{tr} = x/l_c = 0.15$ on the pressure side. The values are chosen in agreement with available TBL-TEN measurement data from the BANC (benchmark for airframe noise computations) workshop[14]. Thus, a validation for the method will at least be possible for the baseline geometry (see Appendix). A far-field boundary condition with the flow values (u_∞ and α) is applied at the outside boundaries. The two-equation SST-k-ω turbulence model as proposed by Menter[15] is used for

the simulation of viscous effects and turbulence statistics. The analysis also includes cases with natural transition from laminar to turbulent boundary layer flow. Therefore the $\gamma - Re_\theta$ transition model is used[16]. Both models are implemented in the DLR flow solver TAU.

2.3 CAA

The CAA calculations are performed using DLR's in house code PIANO[17]. Turbulent noise sources are computed from synthetic turbulence generated by the FRPM code (see Sec. 2.4). In the computational domain this turbulence is coupled with the CAA solver, which is based on the 4th order accurate DRP scheme proposed by Tam & Webb [18]. The synthetic turbulence in conjunction with the RANS mean-flow defines the right-hand side fluctuating source terms of the acoustic perturbation equations (APE[19]), which are a modification of the linearized Euler equations (LEE) so that vorticity or entropy convection is entirely prescribed by the source term whereas acoustic generation and radiation is simulated dynamically. Note, the APE realize a solution to the wave operator of irrotational flow. Together with proper right-hand side volume sources this becomes an acoustic analogy based on that wave operator.
It is argued that the source term mainly acts as a vorticity source term. Sound due to the interaction of vorticity with the trailing-edge is generated as part of the CAA simulation step. The vortex dynamics are dominated by linear contributions to the source terms. Non-linear contributions mainly deemed responsible for sound generation of free turbulent flow are neglected. It is observed that the incorporation of turbulent decay into the source model virtually has no effect on the spectra compared with simulations based on frozen turbulence. Neglecting entropy fluctuations and density fluctuations due to turbulent velocities in low Mach number flows the APE-4 equation system with corresponding right-hand sides reads:

$$\begin{aligned} &\frac{\partial p'}{\partial t} + c_0^2 \boldsymbol{\nabla} \cdot \left(\rho_0 \boldsymbol{v}' + \boldsymbol{u}_0 \frac{p'}{c_0^2} \right) = 0 \ , \\ &\frac{\partial \boldsymbol{v}'}{\partial t} + \boldsymbol{\nabla} \left(\boldsymbol{u}_0 \cdot \boldsymbol{v}' \right) + \boldsymbol{\nabla} \left(\frac{p'}{\rho_0} \right) = \boldsymbol{L}' \ . \end{aligned} \tag{1}$$

The turbulent sources are represented by the fluctuating Lamb vector $\boldsymbol{L}'$. Quantities with subscript 0 denote mean-flow variables whereas the prime indicates fluctuating quantities. The perturbation velocity is represented by $\boldsymbol{v}'$. The fluctuating acoustic pressure p' and fluctuating density ρ' are linked via

$$p' = c_0^2 \rho' \ , \tag{2}$$

where the squared speed of sound c_0^2 is defined by the mean-flow variables (with the isentropic exponent of air $\kappa = 1.4$):

$$c_0^2 = \kappa \frac{p_0}{\rho_0} \ . \tag{3}$$

The APE are solved on a two-dimensional computational domain extending about 6 by 6 chord lengths with the airfoil in the center. An example mesh for the baseline DU-96-W-180 airfoil is depicted in Figures 4 (a) to (c). Note, that for a clearer illustration only every tenth grid line is shown. Bold lines represent the block boundaries. A structured

multi-block mesh is chosen to utilize the parallelized computation with PIANO, where sets of blocks can be computed solely by one CPU. The shown mesh consists of 64 blocks with a total number of approximately 1.1 million cells. In contrast to CFD meshes CAA meshes have a nearly uniform cell density in the far-field region to resolve the acoustic waves. In the actual case, with a resolution of 7 points per wave-length and a reference chord length $l_c = 1m$, frequencies up to maximum frequency of $f_{max} = 5\,\mathrm{kHz}$ can be resolved. For an estimation of the TBL-TEN peak frequency the estimation of Brooks, Pope and Marcolini[3] can be used:

$$St_{peak} = 0.02Ma^{-0.06} \ . \tag{4}$$

Herein St_{peak} represents the peak Strouhal number of the problem and Ma stands for the free stream Mach-Number. The peak frequency can be calculated as:

$$f_{peak} = \frac{St_{peak}\delta^*}{u_\infty} \ . \tag{5}$$

As a first estimation the turbulent boundary layer thickness δ of a flat plate can be used:

$$\delta = \frac{0.37x}{Re(x)^{1/5}} \ . \tag{6}$$

Together with the assumption[20], that the boundary layer displacement thickness δ^* is 30 % of boundary layer thickness δ this yields a peak frequency of $f_{peak} \approx 450\,\mathrm{Hz}$ for the chosen test case parameters (see Sec. 3.1). For the airfoils under investigation, the adverse pressure gradient due to the surface curvature and inflow angle of attack, is supposed to lead to even thicker boundary layers at the trailing-edge resulting in decreased peak frequencies. Thus, the upper limit resolution of $f_{max} = 5\,\mathrm{kHz}$ is still reasonable to capture nearly all parts of the resulting TBL-TEN spectrum.
In Figure 4 (b) the finer resolution around the trailing-edge is visible. This increase of mesh cells is necessary to ensure proper communication of the CAA blocks with the FRPM source patch (indicated in red). The resolution is determined by the minimum integral length scale Λ_{min} of the turbulent boundary layer (see Sec. 2.4). The CAA grid has the same resolution than the FRPM patch in the source patch area (see Fig. 4 (c)) and coarsens towards the outer boundaries to reduce computational effort.

2.4 FRPM

For the preparation of unsteady vortex sound sources a synthetic turbulence method developed at DLR is adopted to force the linearized applied acoustic perturbation equations. The stochastic approach is especially well suited for aeroacoustics purposes, i.e. realizing a '4D' time-space based prediction of fluctuating sources in a restricted volume - the 'source patch'. The 'Random Particle-Mesh Method' (RPM) was first published in 2005[21]. It allows to synthetically realize the time-dependent, turbulent fluctuations from averaged turbulent statistics. It generates Gaussian correlated synthetic turbulence of local integral length scale $\Lambda = c_l/C_\mu\sqrt{k_t}/\omega$ ($c_l \simeq 0.5$, $C_\mu = 0.09$), derived from RANS. The turbulence is generated by spatially filtering a random stochastic field with a Gauss-filter of the aforementioned length scale. In this way an energy spectrum of Gaussian shape is realized. The turbulence is scaled with the local variance (i.e. the turbulence kinetic energy k_t or TKE). The linearized fluctuating Lamb vector that

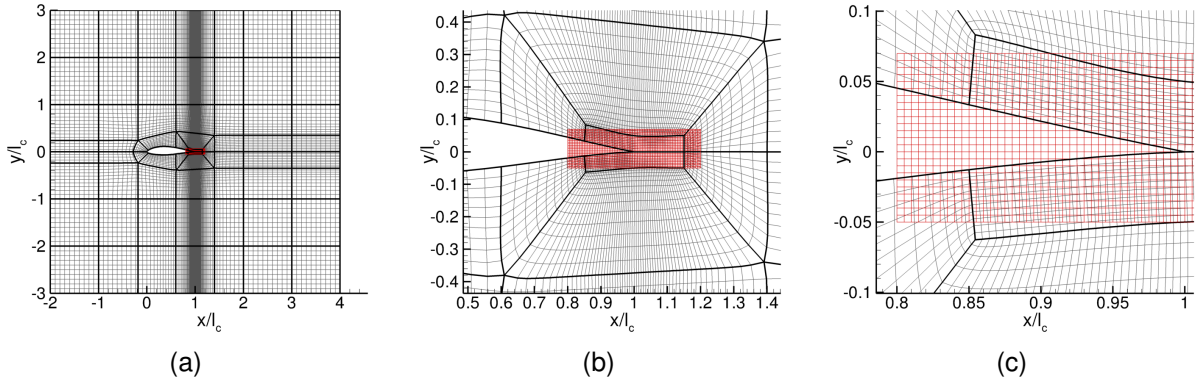

Figure 4: Example DU-96-W-180 CAA mesh with FRPM source patch mesh (shown in red) - for better visualization only every tenth grid line is shown; (a) domain overview; (b) blocks in TE vicinity with FRPM patch; (c) matching resolutions of CAA mesh and FRPM patch).

occurs as the major vortex-force source term on the right-hand side of the momentum equation (Eq. 1) reads:

$$\boldsymbol{L}' = w(\boldsymbol{x})(\boldsymbol{\omega}_0 \times \mathbf{u}' + \boldsymbol{\omega}' \times \mathbf{u}_0) \ . \tag{7}$$

In the above given source term $\mathbf{u}_0$ and $\mathbf{u}'$ are the mean and fluctuating velocity vectors that define the unsteady flow velocity via $\boldsymbol{u} = \boldsymbol{u}_0 + \boldsymbol{u}'$. The local source term weighting is represented by $w(\boldsymbol{x})$. Furthermore, $\boldsymbol{\omega}_0 = \nabla \times \boldsymbol{u}_0$ and $\boldsymbol{\omega}' = \nabla \times \boldsymbol{u}'$ denote the mean and fluctuating vorticity, respectively. The fluctuating velocity field can be decomposed into a solenoidal part associated to the field of fluctuating vorticity $\mathbf{u}^t$ and an irrotational part $\mathbf{u}^a$ associated to volume dilatation, i.e.

$$\mathbf{u}' = \mathbf{u}^t + \mathbf{u}^a, \tag{8}$$

with $\nabla \times \mathbf{u}^t = \boldsymbol{\omega}'$, $\nabla \cdot \mathbf{u}^t = 0$, and $\nabla \times \mathbf{u}^a = 0$, $\nabla \cdot \mathbf{u}^a = \theta'$, where $\theta' = \nabla \cdot \mathbf{u}'$ is the fluctuating dilatation.

The FRPM approach generates the solenoidal velocity field $\mathbf{u}^t$. Its variance is scaled to comply with the RANS turbulence kinetic energy (TKE) distribution, i.e. $\left\langle |\mathbf{u}^t|^2 \right\rangle = 2k_t$ (i.e. the variance will be zero at the wall)[1]. The fluctuating vortical velocity completely comprises fluctuating vorticity. However, the vortex force source term derived from it lacks the acoustic velocity contribution $\boldsymbol{\omega}_0 \times \mathbf{u}^a$. It can be argued that the latter contribution represents a virtual sound source contribution describing refraction of acoustic waves in rotational flow - an effect that is neglected in the simulation of acoustics propagation based on the wave operator of irrotational flow encoded in the APE. To conclude, in the approach of Ewert the volume source terms are modeled by means of RANS and FRPM, defined by

$$\boldsymbol{f} = w(\boldsymbol{x})(\underbrace{\boldsymbol{\omega}_0}_{\text{RANS}} \times \underbrace{\mathbf{u}^t}_{\text{FRPM}} + \underbrace{(\nabla \times \mathbf{u}^t)}_{\text{FRPM}} \times \underbrace{\mathbf{u}_0}_{\text{RANS}}). \tag{9}$$

[1]The solenoidal velocity component $\mathbf{u}^t$ is the one defined by a Helmholtz decomposition (i.e. as induced by Biot-Savart's law based on the given fluctuating vorticity distribution) plus an additional gauge potential $\nabla\varphi$ that satisfies $\Delta\varphi = 0$ and that realizes zero velocity fluctuations at the wall.

The simulations are carried out generating one turbulent 2D 'slice' out of the 3D turbulent field (refer to Ref.[22]) and conducting a CAA simulation on a 2D mesh. The benefit in terms of computational time of this approach goes without saying. It was shown in Ref.[22] that a 2D-to-3D correction has to be applied to the spectrum to correct the 2D simulation for 3D sound radiation. However, the correction does not reveal explicit frequency dependence. Therefore, despite a constant off-set, the procedure provides the correct spectral shape. That is, relative differences in the spectra should be covered and the constant off-set has been removed by calibration of the results with one set of experimental reference data. The simulation presented in this work have been conducted based on a realization of isotropic turbulence, i.e., the FRPM generated fluctuating velocity exhibits a cross-correlation between two points a distance r apart, defined by

$$\left\langle u_i^t u_j^t \right\rangle = \left\langle {u_1^t}^2 \right\rangle \left\{ \left[f(r) - g(r) \right] \frac{r_i r_j}{r^2} + g(r)\delta_{ij} \right\} . \tag{10}$$

The function $f(r)$ is the longitudinal correlation function realized as a Gaussian by FRPM. The function $g(r)$ denotes the corresponding lateral correlation function. Based on the realization of isotropic turbulence, an extension to anisotropic turbulence would be feasible[23, 24].
For all test cases a 800 by 240 cells source patch with the dimensions $x/l_c = 0.4$ by $x/l_c = 0.12$ is used (indicated in red in Fig. 4). The patch is centered at the trailing-edge. Besides the mean flow velocity $\boldsymbol{u}_0$ the patch contains the turbulence kinetic energy k_t as the variance and the turbulent length scale Λ. All values are taken from the previously conducted RANS simulation. Moreover a smooth weighting function $w(\boldsymbol{x})$ with which the source strength is ramped up towards $100\,\%$ at the trailing-edge ($x/l_c = 1$) according to Ref. [25] is chosen. Thus, artificial noise due to the sudden introduction of new sound sources by the patch can be kept to a minimum.

3 Test Case Setup

3.1 Airfoil Geometry

In the present study several variations of geometry and flow parameters and their effect on aerodynamic as well as aeroacoustic performance are evaluated. As the research aims on wind turbine noise prediction and mitigation, a common wind turbine airfoil - the DU-96-W-180[26] is chosen for the baseline setup. The maximum relative thickness $t/l_c = 18\,\%$ is located at a chord position of $x/l_c = 35\,\%$. For a systematic geometry variation a scheme similar to the 4-digit NACA airfoil series approach is chosen. The original thickness distribution from the DU airfoil is first linear scaled to the desired thickness. In a second step the 4-digit NACA mean line according to Ref.[27] is calculated using Equation 11:

$$y_c = \begin{cases} \frac{m}{p^2}\left(2px - x^2\right) & 0 \leq x \leq x_{t_{max}} \\ \frac{m}{(1-p)^2}\left[(1-2p) + 2px - x^2\right] & x_{t_{max}} \leq x \leq 1 \; . \end{cases} \tag{11}$$

The ordinate of the mean line is represented by y_c with the maximum as a fraction of the chord m and its chordwise position p. By variation of m and p it is now possible to adjust the camber and the position of maximum camber for the DU-96-W-180 airfoil

while maintaining its original thickness distribution. The original DU airfoil shows a maximum camber of $m = 0.025$ at a chordwise position of $p = 0.37$. Using this values with the NACA scheme the so produced modified DU airfoil looks quite similar to the original one (see Fig. 5 (a)). A slight deviation in the mean line (see Fig. 5 (b)) can be observed towards the trailing-edge. The rear loading of the original airfoil is thus slightly higher.

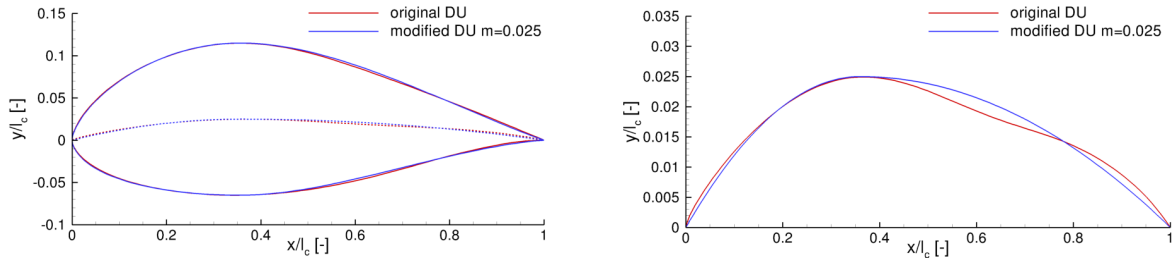

(a) (b)

Figure 5: DU-96-W-180 compared to modified baseline airfoil with NACA mean-line systematic; (a) airfoil geometry; (b) detailed comparison of mean lines.

A relative geometry variation with the above described method is now possible. The modified DU airfoil is thereby considered as the baseline airfoil. A total of 9 airfoils were created with relative thicknesses of $t/l_c = 0.16, 0.18$ and 0.20 and a camber of $m = 0.015, 0.025$ and 0.035 (see Fig. 6). Relative thickness distribution and the position of maximum camber were fixed to the original DU values. The trailing-edge thickness is set to zero for all airfoils in order to simplify the mesh generation process. The geometrical changes were kept to relative subtle amounts in order to retain the aerodynamic performance of the airfoils.

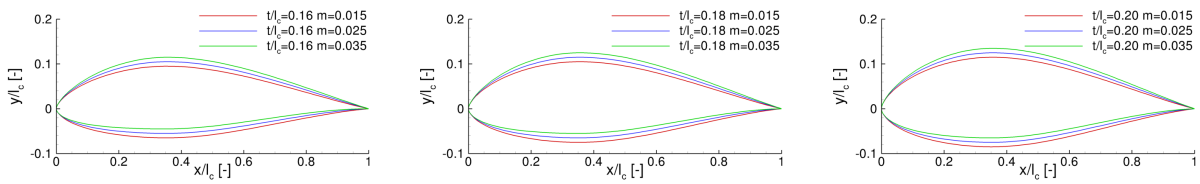

(a) (b) (c)

Figure 6: Airfoil geometries with varied camber for different relative thicknesses; (a) $t/l_c = 0.16$; (b) $t/l_c = 0.18$; (c) $t/l_c = 0.20$.

3.2 Flow Conditions

All airfoils are analyzed for four angles of attack $\alpha = 3°, 4°, 5°$ and $6°$ which are supposed to lie in the linear region of the lift curve. Thus, no separation should be present at the suction side and the only noise mechanism of interest is TBL-TEN. The change of angle of attack allows it to simulate different aerodynamic conditions for each airfoil. Consequently, it is possible to find matching conditions for noise comparisons. For a fair comparison of the airfoil noise contributions it is essential to compare test cases with same aerodynamic performances (for example lift coefficient c_L or glide ratios

(c_L/c_D)). Ambient pressure and temperature are chosen to ISO standard atmospheric conditions. The chord length is set to $l_c = 1\,\mathrm{m}$ and the flow velocity is determined by the desired Reynolds-Number of 3 million[2]. As laminar-turbulent transition plays an important role for the aerodynamic performance two different settings where analyzed for each airfoil. The first setting comprises a fixed laminar turbulent transition at $x_{tr} = x/l_c = 0.12$ on the suction side and $x_{tr} = x/l_c = 0.15$ on the pressure side while the second setting uses a transition model ($\gamma - Re_\theta$) to calculate the natural transition locations. The airfoil surface is supposed to be hydraulically smooth and the turbulence intensity less than one percent. The flow parameters are summarized in Table 1.

Table 1: Used flow parameters

pressure	p_∞	101325	Pa
temperature	T_∞	288.15	K
density	ρ_∞	1.225	kg/m^3
velocity	u_∞	43.82	m/s
chord	l_c	1.0	m
Re number	Re	$3 \cdot 10^6$	$-$
Ma number	Ma	0.129	$-$
angle of attack	α	3; 4; 5; 6	$^\circ$

4 Results and Discussion

For each of the nine airfoils under investigation four angles of attack were analyzed. Additional to that, all cases were simulated with forced and fixed laminar turbulent transition, resulting in total number of 72 combined CFD/CAA simulations. This rather large amount of computations could only be processed using massive automation in the different steps within the simulation procedure. The computational most intensive step is clearly the CAA Simulation which takes about 14 hours on a 16CPU cluster node. All other steps, together with the TAU CFD simulation can be done in less than 2 hours, bringing the overall computational time to around 16 hours per case. For the simulations multiple nodes on the DLR CASE-cluster could be used, keeping the overall computational time within reasonable limits. In the next subsections aerodynamic as well as combined aerodynamic-aeroacoustic results will be shown and discussed.

4.1 Aerodynamics

Fixed transition

Figure 7 shows lift curves for the airfoils in the desired angle of attack range. Laminar turbulent transition was fixed according to the values given in Section 3.2. The linear increase of the lift coefficient c_L with the angle of attack underlines the statement that no suction side separation is present in these cases. One can clearly see, that the airfoil

[2]Typical wind turbine Reynolds numbers in the outer part of the rotor blade are often in a range between 3 and 6 million. The acoustic simulation approach is also capable of higher Reynolds Numbers, but the effects linking geometry and noise emission are supposed to be the same. Therefore only one flow velocity is analyzed so far. If needed, a desired scaling approach can be applied.[8]

camber m indicated by the symbols in Figure 7 (a) is the main influence parameter for the lift. Increasing camber one percent leads to a lift gain of roughly $\Delta c_L = 0.1$. Variations in relative thickness indicated by the line style only show minor influence on the lift coefficient. The 20 % thick airfoil always has the smallest lift compared to thinner airfoils. The effect of lift mitigation by thickness increase is most prominent for strong cambered airfoils ($m = 0.035$; $\Delta c_L = 0.03$) while it diminishes for only slightly cambered airfoils ($m = 0.015$; $\Delta c_L = 0.01$).
Taking a look at c_L versus c_D plots (Fig. 7 (b)) the picture now changes a little bit. While the main driver for the lift coefficient c_L was the airfoils camber, the drag coefficient c_D is primary influenced by the relative airfoil thickness. It is obvious, that thicker airfoils tend to produce more drag than thinner ones. So two effects govern the aerodynamic efficiency of the airfoils determined by the glide ratio (ratio c_L/c_D). Efficiency is thereby increased by either increasing camber or decreasing thickness. This kind of trivial finding will become more interesting when interpreting the aeroacoustic performance of the airfoils.

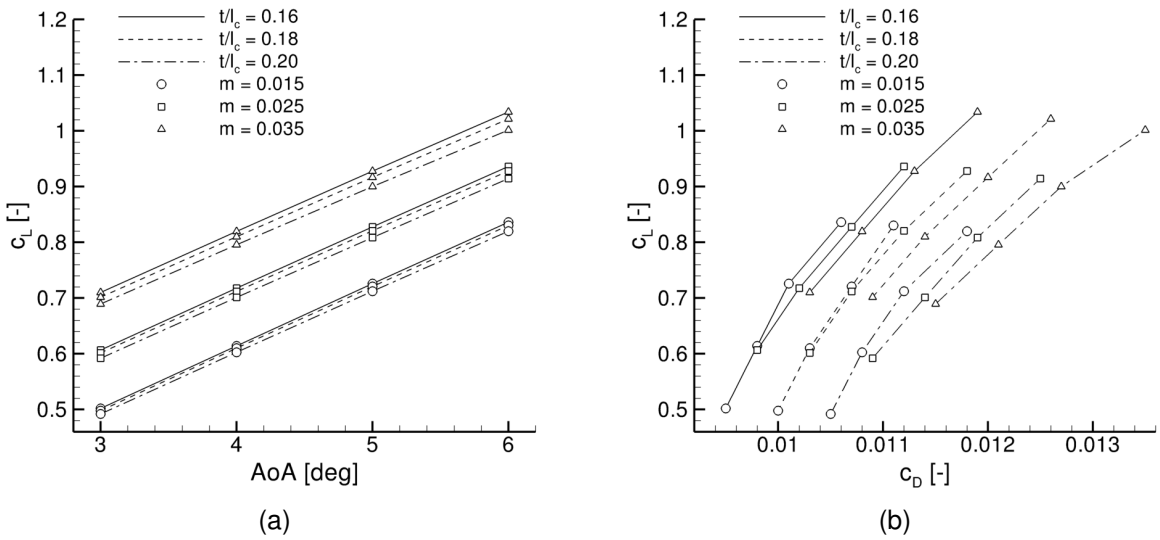

Figure 7: Aerodynamic coefficients for the nine different airfoils for fixed laminar turbulent transition; (a) lift coefficient c_L vs. angle of attack; (b) lift coefficient c_L vs. drag coefficient c_D.

Natural transition

Removing the effect of fixed laminar turbulent transition and instead using the $\gamma - Re_\theta$ transition model reveals the severe influence of the transition on the drag coefficient (see Fig. 8 (a)). While the lift coefficient is almost untouched by the transition, the drag coefficient is nearly halved. From the CFD data it was possible to extract the local wall friction coefficient and find the position where it is rapidly increased, indicating the transition from laminar to turbulent boundary layer flow. The transition position is depicted in Figure 8 (b) for different angles of attack. It can be observed that for increasing AoAs the transition position moves forward on the suction side (due to the increasing adverse pressure gradient) and backward on the pressure side. Thinner airfoils show longer laminar running lengths on the pressure side while the transition

on the suction side is more affected by angle of attack increase, especially for low cambered airfoils which show the strongest decrease of laminar running length.

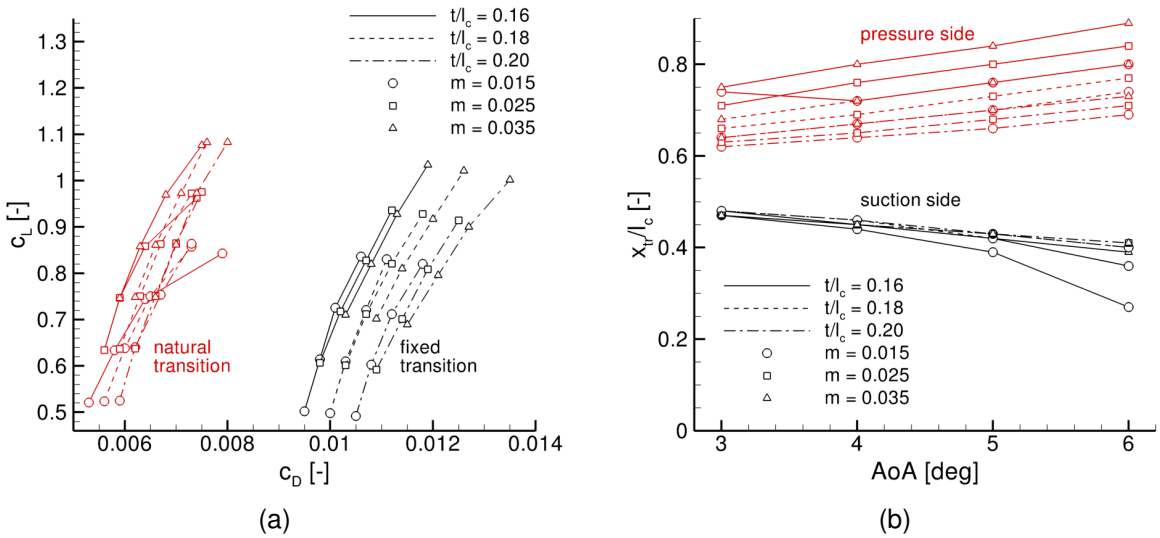

Figure 8: Aerodynamic performance for fixed and natural transition; (a) lift coefficient c_L vs. drag coefficient c_D; (b) location of the transition from laminar to turbulent flow for the natural transition simulations distinguished for pressure and suction side.

4.2 Acoustics

While the aerodynamic results show the expected behavior for 2D airfoil flow simulations the aeroacoustic analysis yields a clearer inside into the TBL-TEN problem. Moreover by having both - aerodynamic and aeroacoustic results - it is now possible to evaluate modifications on both scales and do the trade-off between aerodynamic and acoustic benefits.

The CAA analysis is done in the 2D domain. Figure 9 (a) shows an instantaneous snap shot of the non-dimensionalized fluctuating sound pressure field around the baseline airfoil. The dipole like behavior and the forward inclined directivity of the main radiation as well as the areas with less sound imission in the direction of the chord are clearly visible. The fluctuating sound pressure p' is recorded over time at 360 virtual microphone positions arranged circular around the trailing-edge in a distance of 2.5 chord lengths l_c. For all further investigations the microphone position directly below the trailing-edge ($x/l_c = 1$, $y/l_c = -2.5$) is chosen as the representative position for acoustic results. Figure 9 (b) shows one-third-octave band spectra for the baseline airfoil with varying angle of attack at the desired position. Note, that the shown spectra represent uncorrected values. In order to compare the data to measurement values a 2D to 3D correction as proposed by Ewert et al.[22] has to be applied. Also, it was shown in Ref. [25] that a constant off-set calibration of -4.5 dB has to be used on all simulated CAA spectra to match experimental data in terms of absolute levels. As both corrections are independent of the frequency and only yield a constant shift in sound pressure levels (SPL) they are neglected for the following data because the main focus

is on relative differences between the respective airfoils.[3] In Figure 9 (b) the angle of attack influence on the trailing-edge noise can be seen. Each spectrum possesses two peaks indicated by two humps in the shape of the graphs. The low-frequency peak around $f \approx 350\,\mathrm{Hz}$ is increased and shifted to lower frequencies while the second (lower) high-frequency peak around $f \approx 2500\,\mathrm{Hz}$ is also increased but shifted towards higher frequencies for increasing angles of attack. This indicates the fact the the TBL-TEN spectrum is a result of two independent contributions emanating from the airfoils upper and lower side (see Ref. [28, 3]). The low-frequency peak is thereby caused by the suction side boundary layer and the high frequency peak by the thinner pressure side BL.
As discussed in Section 2.3 the maximum resolvable frequency of the CAA mesh is around $f_{max} = 5\,\mathrm{kHz}$. Therefore values above this frequency need to be excluded in the discussion. Nevertheless, the main part of all spectra lies within the resolvable range of the computational mesh.

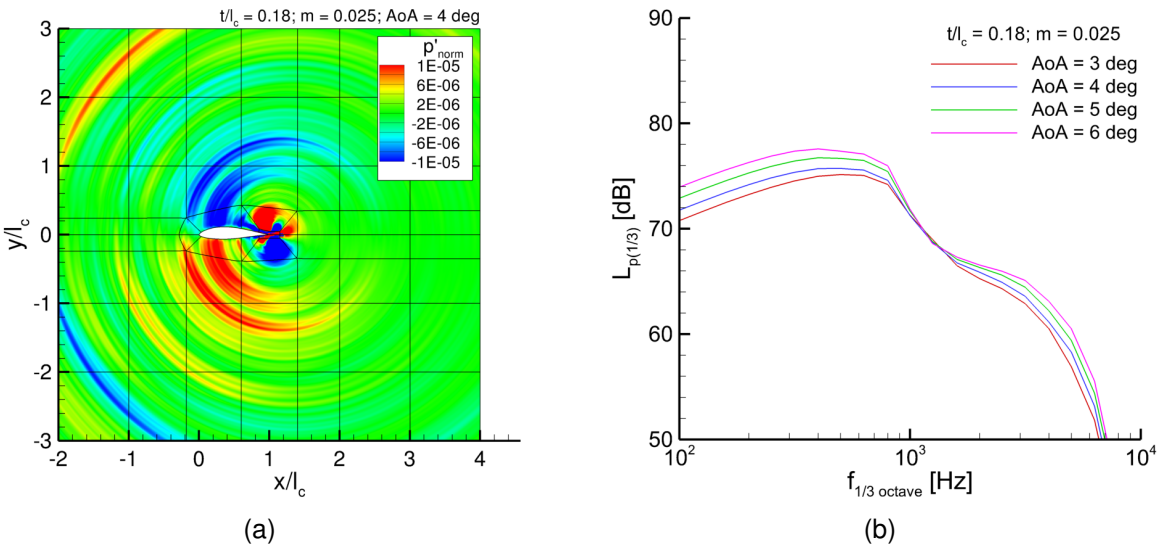

Figure 9: Exemplary aeroacoustic results generated by a CAA simulation conducted with DLR code PIANO; (a) instantaneous plot of fluctuating sound pressure field around the airfoil; (b) resulting one-third-octave band spectra at microphone position 2.5 chord lengths directly below the trailing-edge.

For further data evaluation the overall sound pressure level $L_{p(OA)}$ (OASPL) can be calculated from the single one-third-octave band levels $L_{p(1/3)_i}$ as:

$$L_{p(OA)} = 10 \log_{10} \left(\sum_{i=1}^{n} \frac{10^{L_{p(1/3)_i}}}{10} \right) . \tag{12}$$

Using the above stated equation it is now possible to reduce all acoustic information from the CAA simulation into one value - the overall sound pressure level at the microphone 2.5 chord lengths below the trailing-edge. Such, a combined aeroacoustic aerodynamic analysis based on this value is possible. It is essential that the comparison in terms of aerodynamics is based on a aerodynamic performance indicator. It

[3] A validation of the method comparing corrected CAA values and measurement data for a DU-96-W-180 airfoil is shown in the appendix.

is not useful to compare sound pressure levels for the airfoils under the same angles of attack as c_L and c_D are changed according to AoA changes. A fair comparison of aeroacoustics can only be done if the lift-to-drag ratio or at least the lift is viewed in combination with the overall sound pressure levels. The question is for example, which airfoil produces the minimum TBL-TEN for a given ratio of c_L/c_D or for a given c_L respectively.

Fixed transition

Figure 10 (a) shows overall sound pressure levels compared to glide ratio c_L/c_D for all airfoils under different angles of attack with fixed transition. All airfoils can be operated in a c_L/c_D range between 50 and 90 by adjusting the angle of attack. These aerodynamic performances can be achieved with different noise emissions ranging between 84 dB and 89 dB. It seems, that the airfoil thickness is the main driver for noise emission. While the thin airfoils indicated by the solid lines ($t/l_c = 0.16$) show the smallest overall levels the thick airfoils ($t/l_c = 0.20$) indicated by the dashed-dotted lines show levels which are 3-4 dB higher. For the desired parameter variation of camber and thickness, the airfoil with minimum thickness ($t/l_c = 0.16$) and maximum camber ($m = 0.035$) shows the best performance in terms of glide ratio and overall sound pressure level.

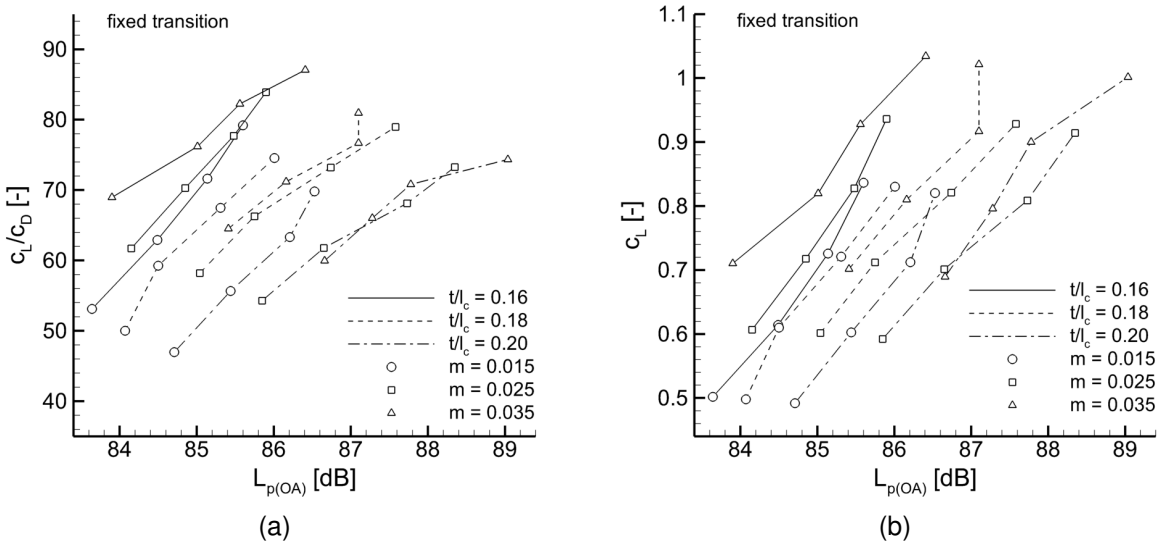

Figure 10: Overall sound pressure levels $L_{p(OA)}$ for different geometries and varying angles of attack compared to aerodynamic parameters for fixed laminar turbulent transition; (a) lift-to-drag ratio c_L/c_D; (b) lift coefficient c_L.

If one compares overall sound pressure levels against lift coefficient (see Fig. 10 (b)) range of $L_{p(OA)}$ variations shortens a bit to 2-3 dB which is due to the fact that the variation in c_L/c_D ratio is mainly influenced by the changing drag coefficient of the airfoils (see Fig. 7 (b)). Nevertheless, it is still possible to produce one and the same lift coefficient with different noise emissions. Also in this breakdown the thin, strong cambered airfoil shows the best performance.

Natural transition

The graphs shown in the previous subsection for fixed laminar turbulent transition are now extended with the simulated values for the natural transition cases. Again, plots for $L_{p(OA)}$ versus lift-to-drag ratio and versus lift coefficient are shown (see Fig. 11 (a) and (b)). The first, most obvious perception is, that a much higher aerodynamic performance (indicated by c_L/c_D ratio) is achieved with less noise emission. This can be explained with the much lower drag coefficients due to the longer laminar running length of the boundary layer flow (see Fig. 8). While the lift is almost the same for the natural transition flow situation, drag is considerably reduced which results in c_L/c_D ratio range of 90 to 140 instead of 50 to 90 for the turbulent flow. Moreover, due to thinner boundary layers caused by the later transition the trailing-edge noise signal is reduced in the magnitude of 3 dB. So airfoils sensitive to transition location changes (airfoils designed for long natural laminar flow) are prone to noise increase by upstream transition movement. Especially in practical wind turbine operation this can be caused by surface contaminations with dust or insect impacts.

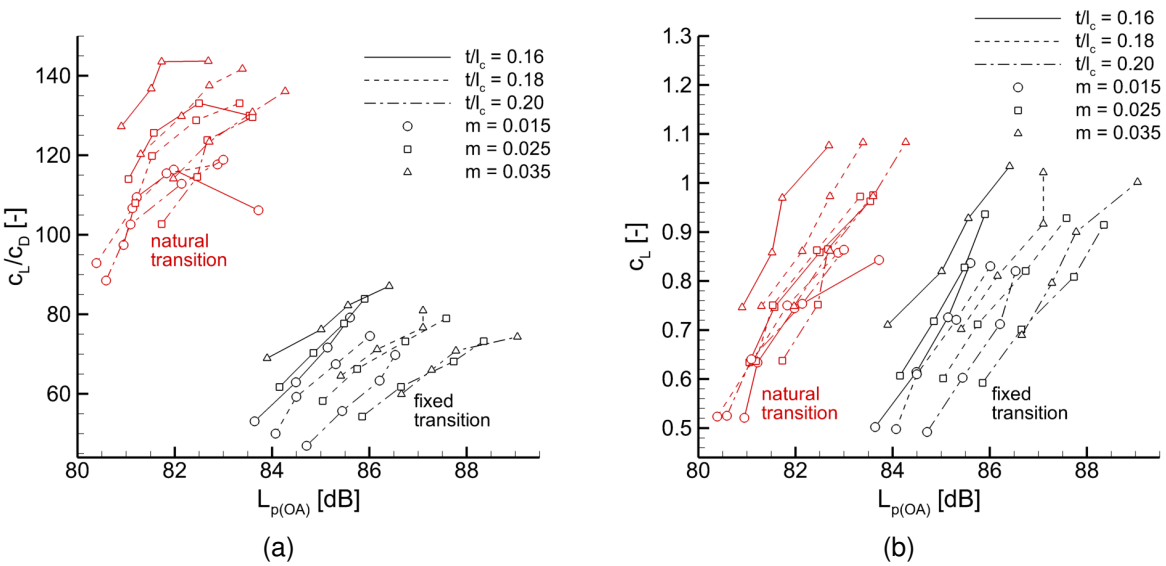

Figure 11: Overall sound pressure levels $L_{p(OA)}$ for different geometries and varying angles of attack compared to aerodynamic parameters for natural laminar turbulent transition; (a) lift-to-drag ratio c_L/c_D; (b) lift coefficient c_L.

Comparing only overall sound pressure levels to lift coefficients (Fig. 11 (b)) one can only see the gain in noise emissions, as the main aerodynamic advantage of the natural laminar boundary layer comes from the reduction in drag. Still, the thin strong cambered airfoil ($t/l_c = 0.16$, $m = 0.035$) shows the best performance but a strong dependence on camber reduction can be observed for this airfoil. This can be explained by the fact, that the thin airfoils exhibits a pronounced decrease in laminar running length with angle of attack increase which is additionally amplified by increasing camber (see Fig. 8 (b)). Thereby two mechanisms come into play. First, the aerodynamic performance in terms of c_L/c_D ratio is reduced and second the thicker boundary layers due to the shorter laminar running length increase the TBL-TEN signal. Generally speaking, the thin airfoils are more critical towards transition locations and tend to lose their good performance faster. Trends seen in the plot of c_L versus $L_{p(OA)}$ indicate that

the range of possible $L_{p(OA)}$ values for generating a certain amount of lift is smaller for natural transition than for fixed transition. But still, a 2 dB difference for the varying geometries can be seen.

4.3 Detailed Assessment of chosen Cases

With the generated database further processing of the CFD and CAA data is possible to identify the noise drivers. Therefore certain representative cases are chosen out of the 72 simulations of the test matrix. They will be compared in detail in the following subsections. To reduce the complexity only cases with fixed laminar turbulent transition locations are investigated. It is argued, that the aerodynamic effects in the boundary layer which are supposed to drive the noise generation process at the trailing-edge are the same in both cases.

Same c_L/c_D ratio with different $L_{p(OA)}$

Three cases were chosen which show the same aerodynamic performance (in terms of c_L/c_D ratio) but different overall sound pressure levels. As the angle of attack is only varied in discrete steps perfect matching of c_L/c_D ratios was not possible. Nevertheless, the cases shown in Table 2 are all closely together with c_L/c_D values around 75. Besides that, the overall sound pressure levels alternate between 85 dB and 89 dB. The thinnest airfoil has the least noise emission while the thickest airfoil shows the utmost values. To reach the same glide ratio as the thin airfoil it has to operate at a higher angle of attack.

Table 2: Test cases with matching c_L/c_D ratio and different $L_{p(OA)}$ values (fixed transition only).

t/l_c [−]	m [−]	α [°]	c_L [−]	c_D [−]	c_L/c_D [−]	$L_{p(OA)}$ [dB]
0.16	0.035	4	0.820	0.0108	76.2	85.0
0.18	0.035	5	0.917	0.0120	76.7	87.1
0.20	0.035	6	1.002	0.0135	74.3	89.0

Figure 12 (a) depicts one-third-octave band SPL spectra for the three cases. According to the diagram, deviation can only be found in the low frequency range (below 1 kHz). In this range all spectra show levels which are quite higher than in the high frequency part and as such will dominate the logarithmic addition according to Eq. 12. As stated in Ref.[3] trailing-edge sound contributions from suction and pressure side can be treated separately and as such are responsible for the different parts of the spectrum. For airfoils which produce positive lift (inclined to the flow or cambered) the thicker suction side boundary layer accounts for the low frequency part and the thinner pressure side BL for the high frequency part.[4] If one compares the pressure distribution around the airfoils (see Fig. 12 (b)) it can clearly be seen, that the graphs are nearly identical for the pressure side but show differences at the suction side (mainly due to higher angles of attack to compensate the drag increase with increasing airfoil thickness). Consequently, differences in the suctions side flow are responsible for the different low

[4]The capability of the CAA simulation approch for this circumstance was shown in Ref. [25]

frequency parts of the spectra. No variation occurs in the high frequency range which is in good agreement with the identical c_p distributions at the pressure side.

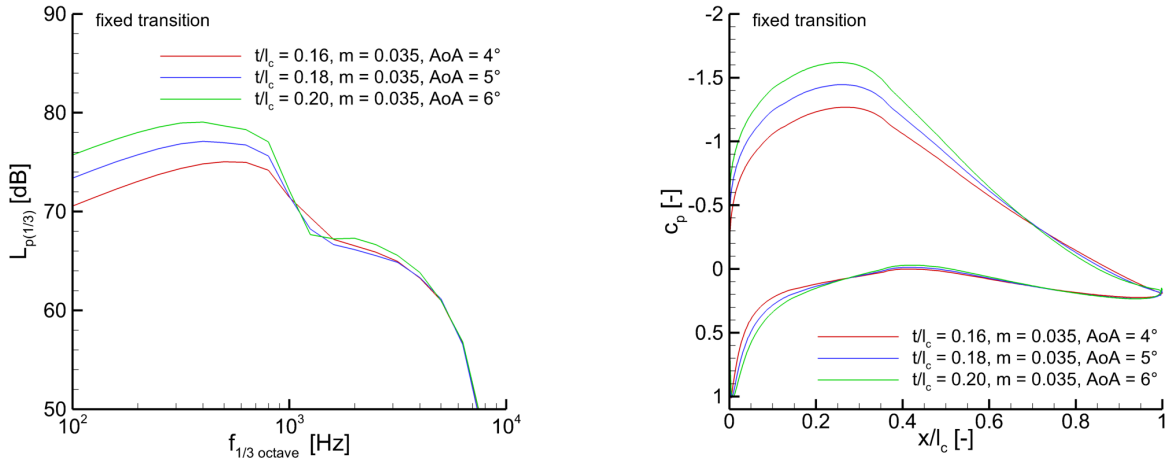

(a) (b)

Figure 12: Comparison of 3 cases with the same c_L/c_D ratio and different $L_{p(OA)}$ values; (a) one-third-octave band spectra at microphone position 2.5 chord lengths directly below the trailing-edge; (b) pressure coefficient for pressure and suction side.

For further analysis, the boundary layer profiles of velocity v_x and turbulence kinetic energy k_t are shown in Fig. 13 (a) and (b). A wider boundary layer with higher k_t values can be observed for the thicker airfoils at the suction side. The order of the TKE peak values thereby corresponds to the order of the maximum SPL values in the one-third-octave band spectra. High turbulence and wide boundary layers cause the higher noise emissions in the low frequency range which is the dominant part of the TBL-TEN spectrum. From a merely acoustic point of view it does make sense to find airfoils which show thin boundary layers at their desired point of operation. Comparing Fig. 12 (b) and Fig. 13 this can be achieved by a low adverse pressure gradient for the suction side pressure regain. As the main function of the airfoils is lift production this fact is somehow intrinsic in the problem statement. Lift cannot be produced without trailing-edge noise, but with elaborate choice of geometry and point of operation a reduction is possible. Clearly, all considerations need to be evaluated also against concurring branches in the rotor blade design process (e.g. structural mechanics or production aspects).

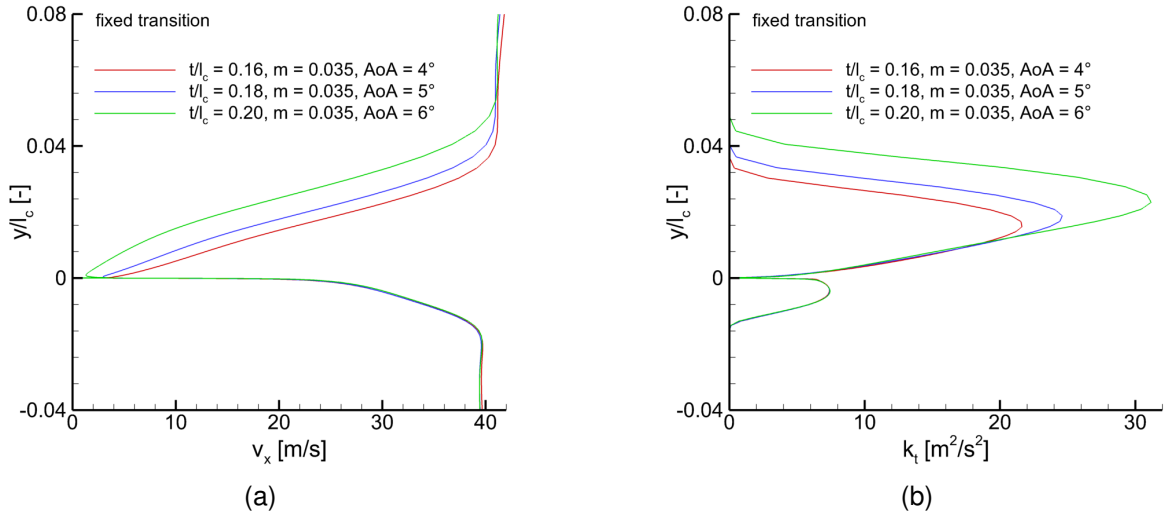

Figure 13: Comparison of 3 cases with the same c_L/c_D ratio and different $L_{p(OA)}$ values directly at the trailing-edge; (a) velocity distribution; (b) turbulence kinetic energy distribution.

Different c_L/c_D ratio with same $L_{p(OA)}$

In contrast to the previous subsection three different cases where chosen for comparison. This time cases with equal noise emissions but different aerodynamic performances are juxtaposed. Representative values can be found in Table 3. Again, three airfoils varying in thickness and operating under different angles of attack were chosen. Thereby, the thinnest airfoil has the highest angle of attack, while the thickest airfoil has the lowest. The overall sound pressure levels nearly match with values slightly below 86 dB. The higher lift coefficient together with the higher angle of attack results in a better c_L/c_D ratio of 83.9 for the thin airfoil compared to 54.3 for the thick airfoil.

Table 3: Test cases with matching $L_{p(OA)}$ values and different c_L/c_D ratio (fixed transition only).

t/l_c [−]	m [−]	α [°]	c_L [−]	c_D [−]	c_L/c_D [−]	$L_{p(OA)}$ [dB]
0.16	0.025	6	0.936	0.0112	83.9	85.9
0.18	0.025	4	0.712	0.0107	66.3	85.8
0.20	0.025	3	0.592	0.0109	54.3	85.9

Figure 14 (a) shows the one-third-octave band SPL spectra for the three different cases. It can be observed that all three spectra show the same levels in the low frequency range below 1 kHz. Slight differences can only be seen in the high frequency range. As the OASPL is dominated by the highest values in the spectrum all OASPL values for the three cases match. The difference in the high frequencies has such a minor contribution that it is not important here. Again, c_p distributions for the three cases are analyzed (see Fig. 14 (a)). For the suction side the paths of the distributions are nearly identical in the pressure regain region downstream of $x/l_c = 0.4$. Only upstream of $x/l_c = 0.4$ more suction is generated by the thin stronger inclined airfoil. As a consequence more lift is produced. Comparing the pressure side distributions it can be seen

that also here, the thin airfoil shows the highest values and as such the strongest lift production. The matching c_p distributions in the aft part of the suctions side seem to indicate similar boundary layer values which prescribe the similar spectra in this region and finally the matching OASPL values. The hypothesis becomes clearer with a closer look on the boundary layer distributions.

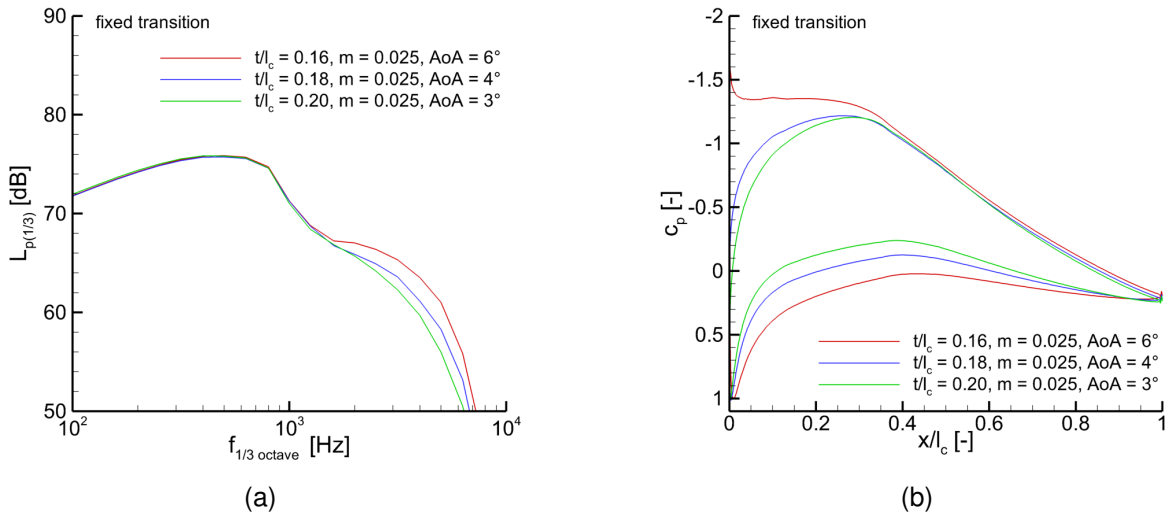

Figure 14: Comparison of 3 cases with different c_L/c_D ratio and the same $L_{p(OA)}$ values; (a) one-third-octave band spectra at microphone position 2.5 chord lengths directly below the trailing-edge; (b) pressure coefficient for pressure and suction side.

Figures 15 (a) and (b) depict the distributions of flow velocity v_x and turbulence kinetic energy k_t across the boundary layer. It can be examined, that for the suction side the airfoils, the velocity as well as the kinetic energy profiles are nearly identical for all three cases. Thus, the same amount of TBL-TEN is present in all three setups. The minor differences seen in the pressure side distributions account for the mismatch in the (not so important) high frequency range of the spectrum. Interestingly the behavior for the pressure side is somehow vice-versa to the one of the suction side. For example, the higher TKE levels lead to the least high frequent noise emission (green line), while the lowest TKE profile (red curve) has the utmost influence on the high frequency noise and shows the highest values. It seems, that flow speed and distance from the trailing-edge become more important for the trailing-edge noise caused by the thin pressure side boundary layer, as the loudest airfoil shows the highest velocities close to the TE. This behavior could not be observed for the suction side.
As the high frequent part of the spectrum generated by the pressure side trailing-edge flow shows an influence on the spectra which is in values so much lower the suction side contribution, the thin airfoil can still be considered the best one in case of noise and aerodynamic efficiency. Generating lift either at the pressure side or respectively in the forward part of the suction side is acoustically the advanced method. Doing this, low noise emission can be achieved with only minor aerodynamic drawbacks. The main focus should thereby lie on the pressure regain of the suction side flow as the low frequency trailing-edge noise contribution is dominating the overall levels.

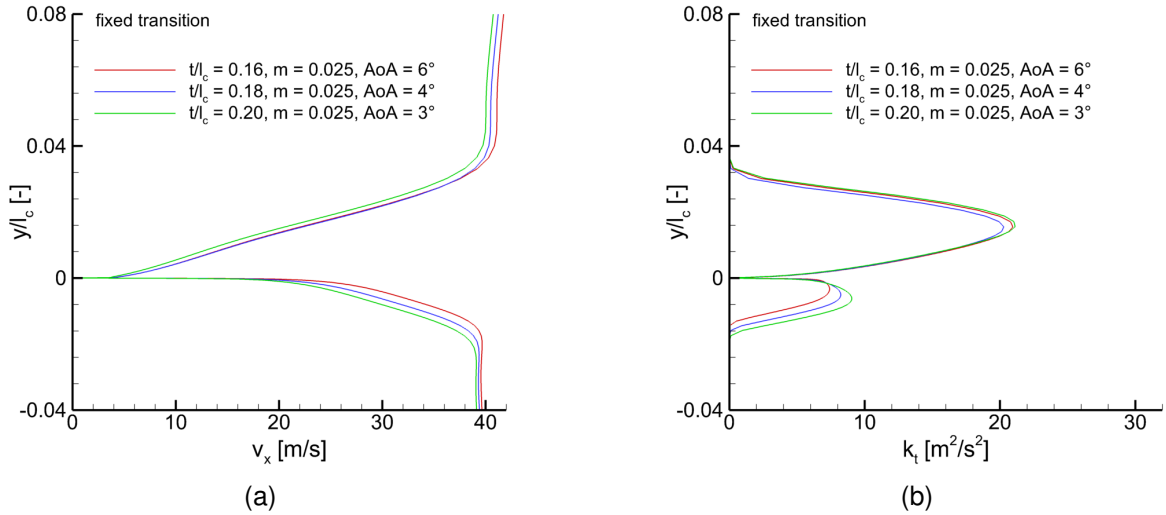

Figure 15: Comparison of 3 cases with different c_L/c_D ratio and the same $L_{p(OA)}$ values directly at the trailing-edge; (a) velocity distribution; (b) turbulence kinetic energy distribution.

5 Summary and Conclusion

A precise and fast method for the simulation of airfoil trailing-edge noise was shown in this paper. The approach relies on a two step hybrid CFD/CAA simulation. The aim was to implement a tool chain which does not rely on semi-empirical noise prediction methods in order to calculate turbulent boundary layer trailing-edge noise. With the shown method it is possible to simulate the time and space resolved fluctuating sound pressure filed around an airfoil under varied flow conditions. With this knowledge overall sound pressure levels can be calculated for different microphone positions and an aeroacoustic evaluation of the airfoil can be conducted. As the results for the two-dimensional simulated case are directly connected to the three-dimensional rotor blade it is argued that advantages on the 2D stage will directly correspond to the full 3D rotor blade in a later rotor blade design. A quieter rotor thereby can be built from noise optimized airfoils. So, in order to save computational resources it is possible to analyze aeroacoustic as well as aerodynamic properties with the prescribed approach. To connect geometrical properties of the airfoil with aerodynamic and acoustic features a systematic geometry variation is undertaken within the test cases. A common DU-96-W-180 wind turbine airfoil was used as a baseline geometry from which a variation of camber and thickness according to the 4-digt-NACA scheme was conducted. With the help of automized mesh generation and setup implementation 72 data sets including aerodynamic data form CFD and aeroacoustic results from CAA were prepared. For a comparison of the different test cases it was essential to incorporate both scales into the evaluation. This means, an acoustically good (low noise) setting does also need to show reasonable aerodynamic properties. To depict this tradeoff, overall sound pressure level were plotted against lift coefficients or glide-ratios (c_L/c_D) respectively. From these studies it can be seen that for the same aerodynamic performance different noise levels with deltas in the range of 5 dB are possible. The detailed data conducted in the CFD and CAA simulation steps allowed it to further analyze the connection between the boundary layer and the connected parts of the trailing-edge noise

spectrum. It was shown that the suction side BL hast the major contribution to the low frequent high value sound pressure levels and as such governs the overall values for most cases. Differences in the pressure side BL do show an influence on the spectrum but in relative subtle values which have only very small influence on the overall values. The major findings of the analysis where, that low TKE values and thin boundary layers show good results in terms of aeroacoustics. The main focus should thereby lie on the suction side. Using strong camber thin airfoil with a low adverse pressure gradient at the suction side will enhance the positive aerodynamic as well as aeroacoustic behavior of an airfoil. Moreover, a longer laminar running length improves not only the aerodynamic characteristics by reducing the drag, also acoustic benefits in the magnitude of 3 dB could be noticed. Thinking about rotor blade surface contamination this fact needs to be kept in mind.
The choice of an airfoil for a wind turbine rotor blade is a challenging task. Various concurrent requirements need to be weighed against each other. With the shown method it was possible to generated guidelines on noise mitigation while keeping aerodynamic efficiency. Still, other aspects like manufacturability and structural properties need to be evaluated in subsequent steps. Nevertheless, the hybrid CFD/CAA approach is able to predict the noise emission with reasonable accuracy towards the complex flow and geometry parameters. It can be used for arbitrary geometries and various flow settings and as such represents a valuable tool in the wind turbine rotor blade design process.

Appendix

Validation of the CAA approach

The validation of the outlined hybrid CFD/CAA method is shown according to available TBL-TEN measurement data from the BANC-II (benchmark for airframe noise computations) workshop[14]. Herein, a DU-96-W-180 airfoil with a chord length of $l_c = 0.3\,\mathrm{m}$, an angle of attack of $\alpha = 4^\circ$ and a flow Mach number of $Ma = 0.173$ was studied. Figure 16 (a) depicts the one-third-octave band spectra recorded 1 m below the trailing-edge. Note, that for the comparison with measurement data a 2D to 3D correction according to Ewert et al.[22] must be applied to the CAA data. Moreover, following the results from Ref. [25] a constant offset calibration of -4.5 dB needs to considered. In contrast to the method described in Ref. [25], no Liepmann turbulence spectrum was used. It was found, that with a sufficient resolution of the patch area and a lower resolveable minium turbulence length scale ($\Lambda_{min} = 0.002$) the underrepresentation of high frequency noise could be remedied.
In Fig. 16 (a) the 3 dB uncertainty of the measurement data is indicated by the error bars. The simulated levels lie within the uncertainty range throughout the whole frequency range. Note, that due to the model scaling ($l_c = 0.3\,\mathrm{m}$) the maximum resolvable frequency is around 10 kHz. The peak frequency around 1 kHz as well as the decay towards higher frequencies and the and the second spectral peak around 8 kHz are correctly reproduced by the CFD/CAA approach. Additionally, results for the semi-empirical BPM code[3] are depicted. Rather large inaccuracy can be observed throughout the whole frequency range with this method due to the geometrical differences form the DU-96-W-180 airfoil to the reference NACA0012 airfoil.
Fig. 16 (b) shows a directivity plot for the simulated overall sound pressure level around

the airfoil. The graph is in reasonable agreement with the theoretical directivity for flat plate trailing-edge noise according to Ref. [29, 3]. The smaller simulation values between $\Theta = 150\,^\circ$ and $\Theta = 210\,^\circ$ are due to the presence of the airfoil in this region which is not considered in the flat plate test case. In order to compare absolute values the theoretical prediction which is normalized to the TE noise radiation in the $\Theta = 90\,^\circ$ direction was multiplied with the absolute simulated values for the $90\,^\circ$ position.

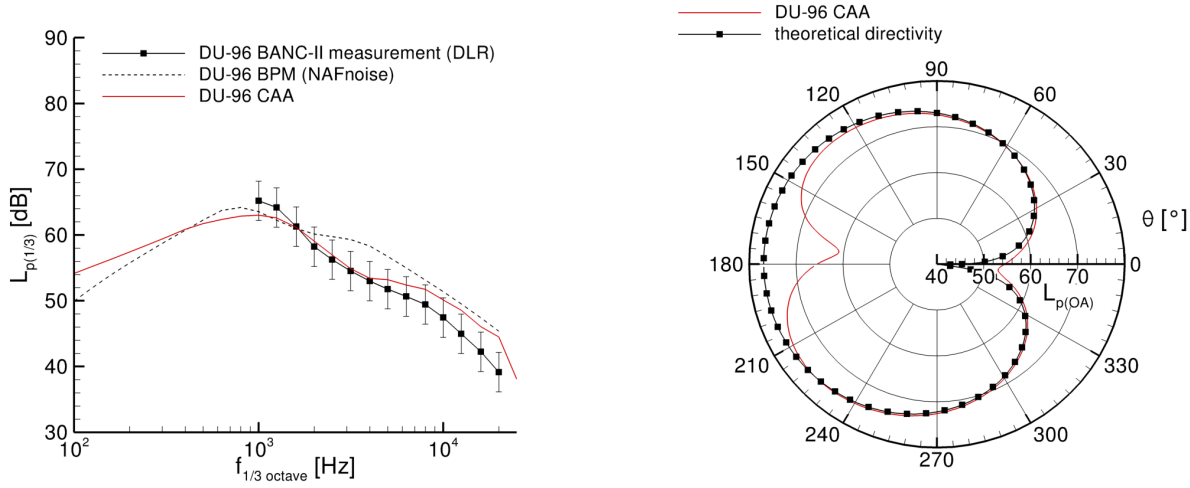

(a) (b)

Figure 16: Validation CAA simulation of original DU-96-W-180 geometry ($Ma = 0.173$, $\alpha = 4\,^\circ$, $l_c = 0.3\,\mathrm{m}$) compared to measurement data from AWB wind tunnel; (a) spectrum CAA, measured, semi-empirical (BPM); (b) directivity of overall sound pressure levels compared to theretical prediction according to Ref. [29, 3].

Acknowledgments

Major parts of the presented work were performed within the framework of a research collaboration between DLR and Nordex Energy[5] with the aim to develop wind turbine noise prediction methods. The author thanks Nordex Energy for their cooperation and the respective funding.

References

[1] GWEC, “Global Wind Report 2013: Annual market update,” 2013.

[2] EWEA, “Wind in Power: 2013 European statistics,” 2013.

[3] Brooks, T. F., Pope, S. D., and Marcolini, M. A., “Airfoil self-noise and prediction,” *NASA Refrence Publication*, , No. 1218, 1989, pp. 1–137.

[5]Nordex Energy is a manufacturer and developer of multi-megawatt wind turbines with a rated power of up to 3.3 MW. As of today, 5500 Nordex wind turbines with a total rated output of more than 9000 MW are installed.

[4] Wagner, S., Bareiss, R., and Guidati, G., *Wind Turbine Noise*, Springer, Berlin and and New York, 1996.

[5] Oerlemans, S., Sijtsma, P., and Méndez López, B., "Location and quantification of noise sources on a wind turbine," *Journal of Sound and Vibration*, Vol. 299, No. 4-5, 2007, pp. 869–883.

[6] Schepers, J. G., Curvers, A. P. W. M., Oerlemans, S., Braun, K., Lutz, T., Herrig, A., Wuerz, W., Mantesanz, A., Garcillán, L., Fisher, M., Koegler, K., and Maeder, T., "SIROCCO: Silent rotors by acoustic optimisation: ECN-M–07-064," 2007.

[7] Lutz, T., Herrig, A., Würz, W., Kamruzzaman, M., and Krämer, E., "Design and Wind-Tunnel Verification of Low-Noise Airfoils for Wind Turbines," *AIAA Journal*, Vol. 45, No. 4, 2007, pp. 779–785.

[8] Herr, M., *Trailing-Edge Noise - Reduction Concepts and Scaling Laws: Dissertation: DLR-Forschungsbericht DLR-FB-2013-32*, Vol. DLR-FB-2013-32, 2013.

[9] Ffowcs Williams, J. E. and Hall, L. H., "Aerodynamic sound generation by turbulent flow in the vicinity of a scattering half plane," *Journal of Fluid Mechanics*, Vol. 40, No. 04, 1970, pp. 657–670.

[10] Ewert, R., "Broadband slat noise prediction based on CAA and stochastic sound sources from a fast random particle-mesh (RPM) method," *Computers & Fluids*, Vol. 37, 2008, pp. 369–387.

[11] Ewert, R., Dierke, J., Siebert, J., Neifeld, A., Appel, C., Siefert, M., and Kornow, O., "CAA broadband noise prediction for aeroacoustic design," *Journal of Sound and Vibration*, Vol. 330, No. 17, 2011, pp. 4139–4160.

[12] Gerhold, T., Galle, M., Friedrich, O., and Evans, J., "Calculation of complex three-dimensional configurations employing the DLR-tau-code," *35th Aerospace Sciences Meeting and Exhibit*, 1997.

[13] Schwamborn, D., Gerhold, T., and Heinrich, R., "The DLR TAU-Code: Recent Applications in Research and Industry," *Proc. of Europ. Conf. on Computational Fluid Dynamics ECCOMAS CFD*, 2006.

[14] Herr, M., Bahr, C., and Kamruzzaman, M., "Workshop Category 1: Trailing-Edge Noise. Problem Statement for the AIAA/CEAS Second Workshop on Benchmark Problems for Airframe Noise Computations (BANC-II): June 7-8 2012, Colorado Springs, Colorado, USA," 2012.

[15] Menter, F. R., "Two-equation eddy-viscosity turbulence models for engineering applications," *AIAA Journal*, Vol. 32, No. 8, 1994, pp. 1598–1605.

[16] Menter, F. R., Langtry, R. B., Likki, S. R., Suzen, Y. B., Huang, P. G., and Volker, S., "A Correlation-Based Transition Model Using Local Variables—Part I: Model Formulation," *Journal of Turbomachinery*, Vol. 128, No. 3, 2006, pp. 413.

[17] Delfs, J. W., Bauer, M., Ewert, R., Grogger, H. A., Lummer, M., and Lauke, T. G. W., "Numerical Simulation of Aerodynamic Noise with DLR's aeroacoustic code PIANO," 2008.

[18] Tam, C. and Webb, J., “Dispersion-Relation-Preserving Finite Difference Schemes for Computational Acoustics,” *Journal of Computational Physics*, Vol. 107, 1993, pp. 262–281.

[19] Ewert, R., “Acoustic perturbation equations based on flow decomposition via source filtering,” *Journal of Computational Physics*, Vol. 188, No. 2, 2003, pp. 365–398.

[20] Anderson, J. D., *Fundamentals of aerodynamics*, McGraw-Hill series in aeronautical and aerospace engineering, McGraw-Hill Higher Education, Boston, 4th ed., 2007.

[21] Ewert, R. and Edmunds, R., “CAA Slat Noise Studies Applying Stochastic Sound Sources Based on Solenoidal Digital Filters,” *AIAA 2005-2862*, Monterey and California, 2005.

[22] Ewert, R., Appel, C., Dierke, J., and Herr, M., “RANS/CAA based prediction of NACA 0012 broadband trailing edge noise and experimental validation: AIAA,” 2009.

[23] Siefert, M. and Ewert, R., “Sweeping Sound Generation in Jets Realized with a Random Particle-Mesh Method,” *AIAA Pap. 2009-3369*, 2009.

[24] Ewert, R. and Dierke, J., “Stochastic approaches to airframe noise prediction,” *Accurate and efficient aeroacoustic prediction approaches for airframe noise; VKI Lecture Series 2013-03*, 2013.

[25] Rautmann, C., Dierke, J., Ewert, R., Hu, N., and Delfs, J., “Generic Airfoil Trailing-Edge Noise Prediction using Stochastic Sound Sources from Synthetic Turbulence,” *20th AIAA/CEAS Aeroacoustics Conference*, edited by AIAA, 2014.

[26] Timmer, W. and Rooij, R., “Summary of the Delft University Wind Turbine Dedicated Airfoils,” *41st Aerospace Sciences Meeting and Exhibit*, 2003.

[27] Eastman, Jacobs, N., Kenneth, E., Ward, E., and Pinkerton, R. M., “The Characteristics of 78 Related Airfoil Sections from Tests in the Variable-density Wind Tunnel: NACA Rept. No. 460,” 1933.

[28] Brooks, T. and Hodgson, T., “Trailing edge noise prediction from measured surface pressures,” *Journal of Sound and Vibration*, Vol. 78, No. 1, 1981, pp. 69–117.

[29] SCHLINKER, R. and AMIET, R., “Helicopter rotor trailing edge noise,” *7th Aeroacoustics Conference*, 1981.